A framework for evaluating steel loss from the evolution of corrosion-induced deflections in reinforced concrete beams with

Engineering Structures 317 (2024) 118593

Contents lists available at ScienceDirect

Engineering Structures

journal homepage: www.elsevier.com/locate/engstruct

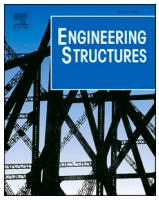

A framework for evaluating steel loss from the evolution of corrosion-induced deflections in reinforced concrete beams with non-uniform reinforcement corrosion

David Dackman [a,b,*], Carlos G. Berrocal [a], Rasmus Rempling [a,c], Ignasi Fernandez [a]

[a] Chalmers University of Technology, Division of Structural Engineering, Göteborg 41296, Sweden
[b] WSP Sverige AB, Fabriksgatan 2, Göteborg 41250, Sweden
[c] NCC Sverige AB, Drakegatan 10, Göteborg 41250, Sweden

ARTICLE INFO

Keywords:
Reinforced concrete
Corrosion
Deflection
Distributed Optic Fiber Sensing (DOFS)

ABSTRACT

Describing corrosion propagation throughout the corrosion process, prior to the extraction and assessment of reinforcement bars, is challenging. In this paper, a framework is proposed for describing corrosion propagation from corrosion-induced variations in deflection for reinforced concrete beams, based on the experimental results of beams simultaneously subjected to either an imposed relative displacement or cyclic loading along with accelerated corrosion through impressed current. Strain measurements from distributed optical fiber sensors were used to calculate the deflection and crack distribution over time. Given the characterization of the initial current density, the framework allowed for the calculation of corrosion development based only on the measured corrosion-induced deflections. The framework was verified, as revealed by the strong agreement between the pit volume loss obtained from 3D scanning of the reinforcement bars and the losses calculated using Faraday's law. Moreover, a second mechanism contributing to corrosion-induced variations in deflection, in addition to the reduced stiffness due to pitting corrosion, was observed for the case with cyclic loading and attributed to bond degradation. Furthermore, for load cycles with similar load level, it was shown that the increase in deflection occurred only when there were intermediate load cycles with a higher load level, suggesting that the assumed bond degradation occurs only when the load surpasses a previous threshold.

1. Introduction

Today, reinforced concrete (RC) stands as the predominant construction material for infrastructure, with significant challenges arising from aging structures, ongoing degradation and the increasing level of traffic loads. Replacing all deficient structures is neither economically nor environmentally feasible. Therefore, it is essential to extend their service life through proper maintenance and condition assessment tools.

Reinforcement corrosion is, among the various deterioration mechanisms of RC, the most widespread and costly one [1]. The initiation of corrosion usually occurs when the protective passive layer on the surface of the reinforcement bar is broken, either due to carbonation or chloride ion ingress. Consequently, there is a reduction of both cross-sectional area and steel-concrete bond [2,3].

The effect of corrosion on the structural behavior of RC has received significant attention in the recent decades. One of the few studies in which the long-term serviceability performance of naturally corroded RC beams has been investigated is that by Zhang et al. [4], where the authors conducted a comprehensive long-term experimental study on the impact of corrosion on the serviceability performance of RC beams subjected to constant loads in three-point bending. Their findings, based on beams exposed to a chloride environment for 14–23 years under service loading, revealed that in the early cracking stage with localized pitting corrosion, bond loss was the primary factor influencing beam deflection. The loss of cross-sectional area became a significant factor only in a later stage when the corrosion was generalized and the bond had already been lost.

In contrast to natural corrosion, accelerated corrosion tests provide a means to reduce testing times and rapidly acquire information on material deterioration [5]. When initiating corrosion through an impressed current, the loss of steel can be estimated using Faraday's law. However, prior studies have indicated a variance, with experimental results of

* Corresponding author at: Chalmers University of Technology, Division of Structural Engineering, Göteborg 41296, Sweden.
E-mail address: david.dackman@chalmers.se (D. Dackman).

https://doi.org/10.1016/j.engstruct.2024.118593
Received 27 February 2024; Received in revised form 29 May 2024; Accepted 7 July 2024
Available online 24 July 2024

mass loss determined through the gravimetric method proving lower than the theoretically calculated values based on Faraday's law [6,7].

Extensive research has been conducted to study the serviceability performance of RC structures subjected to accelerated corrosion. The impact of simultaneous reinforcement corrosion and sustained loading on the structural performance was studied by Du et al. [8]. RC beams were subjected to service loads in three-point bending and all beams, except one, were simultaneously exposed to accelerated corrosion through impressed current. The results revealed a more rapid increase in the time–dependent deflections for the corroded beams compared to the non-corroded reference beam. Furthermore, in a subsequent load-deformation test, an anticipated ductile failure was replaced by a less ductile or even brittle failure for the corroded specimen.

Stein et al. [9] conducted a study on the combined effects of corrosion and cyclic loading in RC beams under four-point bending. Low and high levels of corrosion, with 3–5 % and 8–11 % mass loss, respectively, were achieved by accelerated corrosion using impressed current. The results indicated that the average vertical displacement increased less with the number of cycles for the beams with a low corrosion level, in contrast to the uncorroded reference beams, possibly due to enhanced bond resulting from increased radial pressure caused by the corrosion products. However, larger displacements were observed in the beams with a high level of corrosion in comparison to both the uncorroded beams and those with a lower corrosion level.

The bond behavior between reinforcing steel and the surrounding concrete, for members subjected to cyclic loading and corrosion, has been investigated in several studies. Fang et al. [10] carried out pull-out tests to study the bond stress-slip response for different corrosion levels and loading histories. The findings indicated that the bond strength increased with the level of corrosion up to a maximum point, beyond which higher corrosion levels led to a substantial reduction in bond strength. In another study by Oh et al. [11], three different levels of bond stress, each subjected to a varying number of load cycles, were considered to investigate bond-slip behavior in pull-out tests. The outcomes revealed that the bond strength and slip at the peak bond stress were not significantly influenced by cyclic loading in the absence of bond failure. However, the slip and residual slip increased with the number of load cycles. Moreover, the increase of bond stress after cyclic loading became sharper as the number of repeated cycles increased and approached the ultimate bond stress under monotonic loading. The effects of corroded stirrups on the bond behavior of the tensile reinforcement were studied by Zhou et al. [12]. 57 specimens with corrosion levels ranging between 0–20 % were tested in either monotonic pull-out loading tests or constant or varied amplitude cyclic loading tests. Comparisons to other experimental studies with similar test setups showed that the bond strength is affected similarly, though less severely, by stirrup corrosion compared to rebar corrosion.

Given the significant impact of corrosion on structural performance and the large associated costs, conducting condition assessments to assess corrosion-induced damage is crucial. However, current condition assessment strategies rely on labor-intensive and time-consuming on-site inspections. The information obtained from such inspections is often limited and subjective, resulting in a poor correlation between the data and the actual state of degradation. This discrepancy leads to significant uncertainties. Therefore, the development of assessment methods and monitoring systems capable of providing an accurate description of the structure's condition could enable early detection of structural degradation.

Distributed optical fiber sensors (DOFS) present several advantages over conventional structural health monitoring systems, including compact size, electromagnetic field immunity, remarkable sensitivity and corrosion resistance. Significant technological advancements in recent years have expanded the field, demonstrating the feasibility of employing DOFS for monitoring performance indicators (PI), such as deflection, crack position and crack widths, as evidenced by previous studies [13,14]. The same authors also successfully provided detailed heat maps for the global and principal strain fields in D-regions of a wall element by applying DOFS in a multilayer configuration [15].

Bado et al. [16] investigated the bond stress and slip between the concrete and steel bars by gluing DOFS to grooves carved longitudinally into the reinforcement bars, in both cracked and uncracked RC tensile members. In comparison with the predictions from Model Code 2010, the DOFS measurements consistently indicated higher bond stresses for similar slips.

In a study by Fan et al. [17], the volume of the corrosion products in concrete members was evaluated using strain measurements obtained from sensors deployed in a helical pattern on the steel bars. The corrosion process of the steel bar displayed three stages according to the DOFS strains, consistent with the electrochemical test data measuring the open circuit potential.

Despite promising results regarding the monitoring of PI by DOFS, studies correlating these measurements with corrosion-induced damage are scarce. This paper reports the results of an experimental investigation of the correlations between localized pitting corrosion and deflection measured by DOFS and aims to propose a framework for describing corrosion propagation from corrosion-induced variations in deflection. The framework provides a novel approach to describe how the volume loss due to pitting corrosion develops throughout the corrosion process based on deflections obtained from DOFS readings, and to the authors' knowledge DOFS measurements have not yet been used for that purpose.

2. Experimental program

The tests of the four beams presented in this paper are part of larger experimental program that involves six large-scale RC beams, devised to explore the potential of DOFS in evaluating the performance of RC beams subjected to long-term loading and deterioration. After the initial pre-cracking, four beams were divided into two groups, with one group subjected to an imposed relative displacement and the other to cyclic loading, while simultaneously undergoing accelerated corrosion through impressed current. The most important aspects of the experiment are described below and further details regarding the test setup and results from the long-term loading prior to the corrosion phase can be found in [14].

2.1. Geometry and reinforcement layout

The study comprised RC beam specimens with a rectangular cross-section of 200 × 250 mm and a length of 3 m. Three ∅16 mm bars at the bottom and two ∅10 mm bars at the top were utilized as longitudinal reinforcement. Additionally, on each side of the beams, six ∅8 mm stirrups with a spacing of 200 mm were provided. All reinforcement was made of normal ductility carbon-steel (B500B) with a nominal yield strength of 500 MPa. To enhance anchorage, the bottom bar ends were bent upward. Furthermore, as part of the accelerated corrosion procedure, impressed current was applied, requiring the bars at one end to protrude from the concrete surface to facilitate electrical connectivity. The reinforcement layout and beam geometry are illustrated in Fig. 1.

The beams were cast using a concrete mix with a water-to-cement ratio of 0.45, which included sulfate-resistant Portland cement with moderate heat development and low C3A content. Prior to the pre-cracking, the beams were stored in an indoor environment for 15 days. Subsequently, they were kept within the same indoor environment for an additional six months before the initiation of the long-term loading. Tests carried out in accordance with EN 12390–3:2009 [18], on three 150 mm cubes yielded an average concrete compressive strength of 68.2 MPa (CoV = 5.6 %) at 28 days.

2.2. Test setup and instrumentation

The beams underwent loading using a four-point bending setup. To induce cracking prior to the long-term loading, the beams were

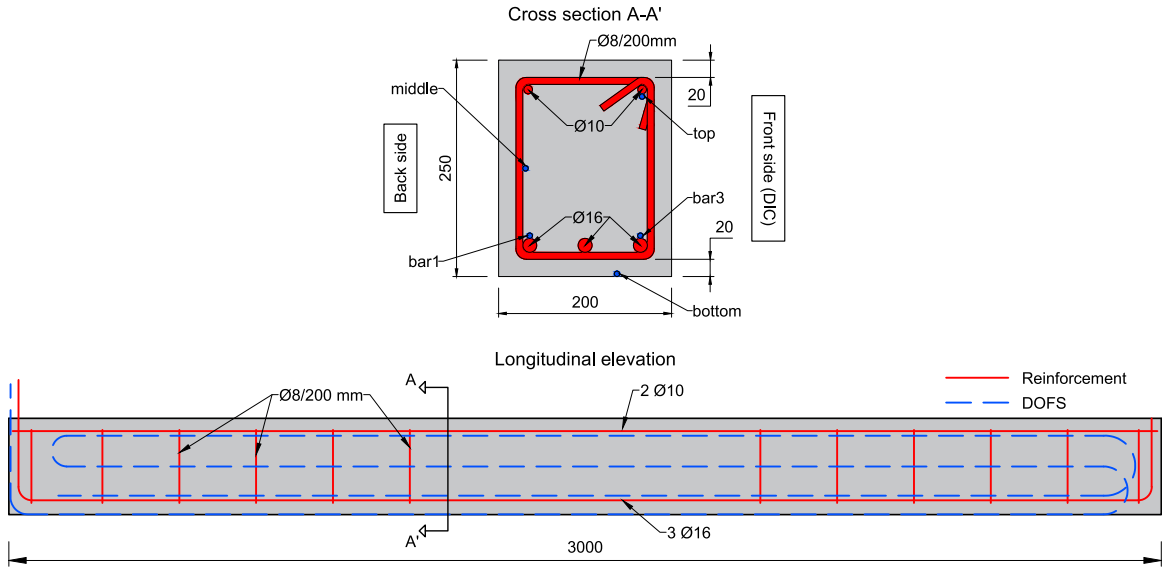

Fig. 1. Reinforcement layout, DOFS configuration and geometry of the beam specimen (all measurements in mm).

subjected to two load cycles of 60 kN, corresponding to approximately 30 % of the anticipated ultimate capacity.

During the long-term loading, the beams were clamped together and divided into two groups according to the setup illustrated in Fig. 2a. The tensile reinforcement of the bottom beam was facing upwards by turning the beam upside down, while the top beam was subsequently placed on support plates, resting upon the bottom beam, at a distance of 2700 mm. Clamping devices were attached to introduce the load at two points, spaced 900 mm apart. The eccentricity of the system supports, due to limitations of the test setup location, did not impact the boundary conditions at the steel roller and load cell.

For the set of beams subjected to an imposed relative displacement, threaded bolts were screwed into the clamping devices, cf. Detail B in Fig. 2a, and tightened to impose a sustained relative displacement between the two beams. To ensure a symmetric load distribution, three load cells were placed, two at the loading points, and the third at one of the supports. The variation in load resulting from changes in the beam stiffness, either due to creep or corrosion, was not adjusted during the test, thereby keeping a constant relative displacement between the beams throughout the test.

In the case of cyclic loading, a hydraulic cylinder was placed between each clamping device and the loading plates of the top beam, cf. Detail A in Fig. 2a. The loading procedure followed a square wave signal, with random variations of both the amplitude and duration within a specified range, according to Fig. 2b. The maximum load per cycle ranged from 10 to 36 kN for each cylinder, with pulse durations spanning from 1 to 6 h. Conversely, a load of 6 kN and an interval of 1 h were kept constant between pulses.

After subjecting the beams to an imposed relative displacement and cyclic loading for a duration of 96 days, an impressed current was applied to the bottom beam to initiate the corrosion process. The accelerated corrosion configuration, as illustrated in Fig. 2c, was specifically selected to create a non-uniform distribution of corrosion. Utilizing a DC power source, the applied current was controlled throughout the entire test duration. The tensile reinforcement bars were electrically connected with each other and to the positive terminal of the power source. Placed on the tensile surface between the loading points, a copper mesh served as the external cathode, which was connected to the negative terminal of the power source. To maintain the electrolytic connection between the reinforcement and the external cathode, cloth pieces covering the copper mesh were regularly wetted. Every half hour, a chloride solution of 0.5 % NaCl (by weight) was pumped for five minutes from a pool beneath the beam. A current of 0.1 A was initially applied for five weeks, followed by two weeks of no current and ultimately resumed for an additional two weeks. Localized pitting corrosion was anticipated due to the presence of bending cracks in combination with the externally placed cathode, as the cracks would provide paths of least resistance. Therefore, pitting corrosion was expected at the intersection of the reinforcement and the cracks.

Strain variations along the beams were continuously monitored with DOFS. For each beam, a single DOFS was deployed in a multilayer configuration along the beam's length, strategically positioned at five different locations of the beam's cross-section according to Fig. 1 and fixed in place with electric tape. A robust cable, BRUsens V9, from Solifos was used. The cable is composed by an external polyamide cladding of 3.2 mm in diameter, a steel stube with a diameter of 0.9 mm and a multi-layer buffer, which helps the strain transfer, surrounding the 250 μm single mode optical fiber.

The Optical Distributed Sensor Interrogator (OdiSI) 6000 series from Luna Inc. was used for data acquisition. The sample rate was set at one measurement every 10 min, while the highest spatial resolution available at the time between the measuring points provided by the interrogator was chosen, namely 2.6 mm. However, a cubic Hermite polynomial interpolation, with a spatial resolution of 10 mm, was applied on the raw data before the analysis of the results to reduce the data volume while maintaining accuracy.

In addition, Digital Image Correlation (DIC) was employed to measure deformations, strain fields and the development of crack widths on one of the lateral sides. This involved periodic image capture using two Fujifilm X-T30 digital cameras. The resulting images had a resolution of 26 megapixels, measuring 6240×4160 pixels, with each image covering a region of the central part of the beams of approximately 1.2×0.8 m, providing a spatial coverage of 0.19 mm/pixel. For the beams subjected to cyclic loading, images were captured every 15 min, while for the beams subjected to an imposed relative displacement, images were taken every two hours. Subsequently, the images underwent processing and analysis using the formerly open-source software GOM Correlate.

2.3. *Characterization of the resulting rebar corrosion*

Upon completion of the accelerated corrosion test, the corroded beams were detached from the testing rig, after which the concrete cover on the tensile side was removed, revealing the reinforcement bars.

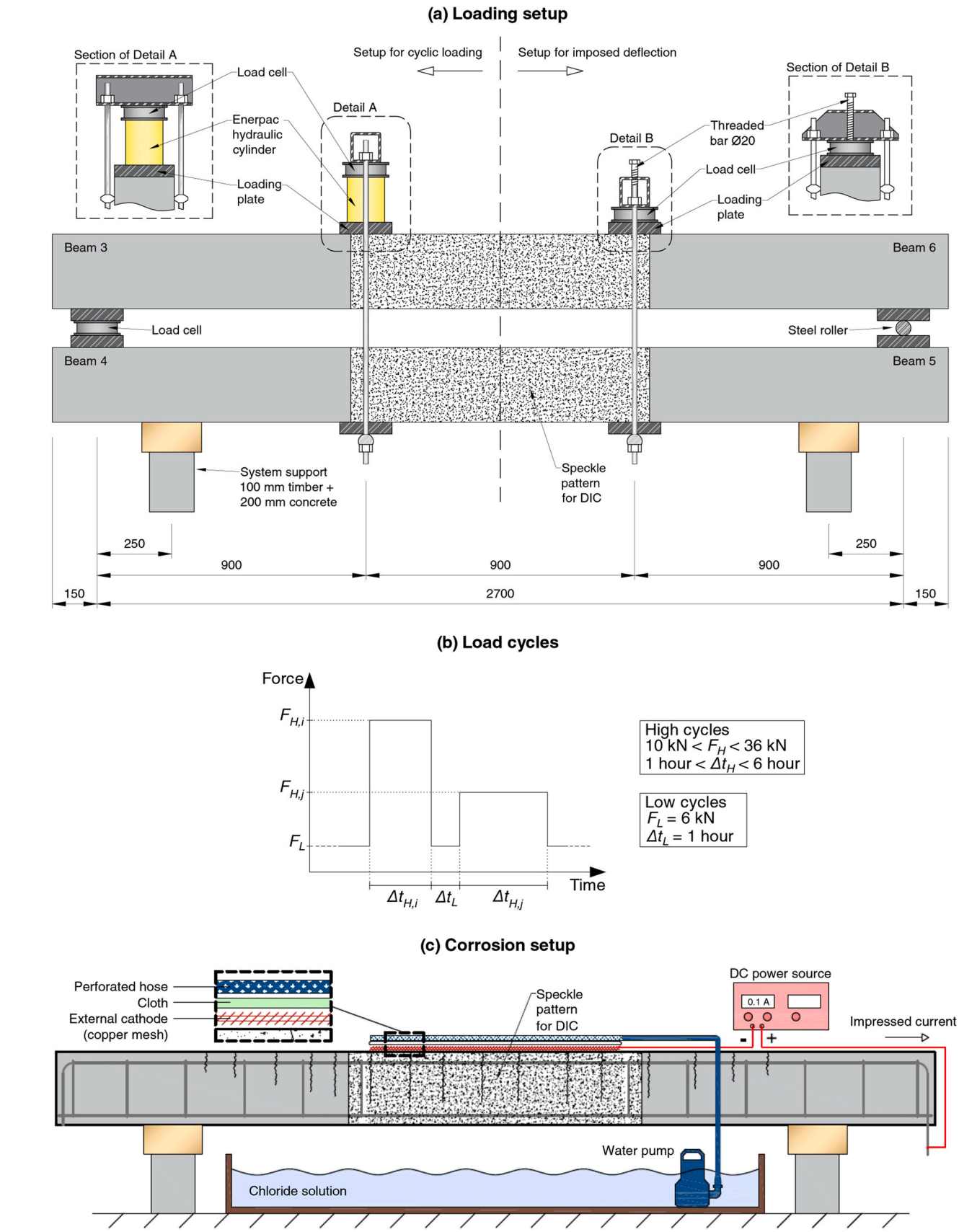

Fig. 2. **(a)** Long-term loading setup; **(b)** Definition of the loading procedure for the cyclically loaded beams; **(c)** Accelerated corrosion setup utilizing impressed current (all measurements are in mm) (after [14,19]).

Focusing on the central part of the beams affected by corrosion, one-meter segments of the rebar were cut out using a water-cooled circular saw. The residual corrosion products were then removed through a sandblasting process, as described in [20].

The assessment of the local corrosion level along the length of the rebar involved 3D scanning of the clean reinforcement bar segments utilizing a portable Handy Scan 700™ laser scanner from Creaform. The outcome was presented in the form of a 3D point cloud, with an accuracy of 30 μm and a maximum spatial resolution of 0.05 mm.

Following the surface interpolation of the 3D point cloud according to [2], a description of the varying cross-sectional area along the length of the bar was provided by integrating the area enclosed by the surface points. Combined with a reconstructed uncorroded reinforcement bar, the local corrosion level μ [%] was defined according to Eq. (1):

$$\mu = \frac{A_0 - A_{corr}}{A_0} \cdot 100 \tag{1}$$

where A_0 is the uncorroded cross-sectional area and A_{corr} is the corroded cross-sectional area.

The total volume loss was obtained by integration of the local sectional loss over the bar length according to Eq. (2):

$$C_{tot,scan} = \int_0^{L_{bar}} (A_0(x) - A_{corr}(x))dx \tag{2}$$

where L_{bar} is the extracted bar length.

Moreover, the calculation of the average corrosion level was conducted over the mean crack spacing. The identification of localized pitting regions, induced by the chosen accelerated corrosion setup, was then defined according to [19], where the pit length was defined as the distance at which the local corrosion level exceeded the average corrosion level. Subsequently, the pit corrosion volume $C_{pit,scan}$ could be determined by integration of the local sectional loss over the pit length according to Eq. (3):

$$C_{pit,scan} = \sum_{i=1}^{n_{pit}} \int_{x_{pit\_start_i}}^{x_{pit\_end_i}} (A_0(x) - A_{corr}(x))dx \tag{3}$$

where n_{pit} is the total number of pits and $L_{pit} = x_{pit\_end} - x_{pit\_start}$ is the pit length.

3. Framework for describing corrosion propagation from corrosion-induced variations in deflection

The aim of this study was to establish a correlation between the variation in corrosion-induced deflections over time and the total ongoing corrosion damage. The loss of steel over time was estimated using Faraday's law following the methodology presented in [21].

The calculation of the final corroded steel volume involved the application of an underlying hypothesis and two assumptions. The underlying hypothesis is that the attribution of any observed variation in deflection is solely due to corrosion at the pits in the cracks, which entails proportionality between deflections and the corrosion losses. The first assumption is that there is an initial stage, before longitudinal cracking occurs, where all corrosion is concentrated at the cracks. The second assumption is the existence of an influence region around the pit that governs variations in the deflections, i.e. an effective pit length at each crack, which furthermore does not change over time.

When a constant impressed current is applied to initiate corrosion, the mass loss of steel Δm can be estimated with Faraday's law, according to Eq. (4):

$$\Delta m = \frac{MIt}{zF} \tag{4}$$

where M is the atomic weight of iron, I is the current, t is time of applied current, z is the valency of Fe and F is the Faraday's constant.

However, due to the discrepancy between theoretical and actual steel losses, as described in [6,7] with the actual losses ranging between 57 % and 67 % of the theoretical losses, an effective impressed current I_{eff} was calculated employing Faraday's law and the total measured volume loss obtained from the 3D scanning, as stated in Eq. (5):

$$I_{eff} = \frac{C_{tot,scan}}{C_{tot,Faraday}} \bullet I = \frac{C_{tot,scan}}{\frac{\Delta m}{\rho}} \bullet I = \frac{C_{tot,scan}}{\frac{Mt}{\rho F z}} \tag{5}$$

where $C_{tot,scan}$ is the total corrosion volume for all three bars obtained from the 3D laser scanning, $C_{tot,Faraday}$ is the total corrosion volume according to Eq. (4) and ρ is the density of iron.

Based on the first assumption, the current density at the initiation of the corrosion process, i_1, can be calculated according to Eq. (6), as all the current is assumed to go through the pits at the affected cracks.

$$i_1 = \frac{I_{eff}}{S_{pit}} = \frac{I_{eff}}{\phi\pi\sum L_{pit}} \tag{6}$$

where S_{pit} is the surface area subjected to corrosion, ϕ is the diameter of the steel bar before corrosion and $\sum L_{pit}$ is the sum of all the individual pit lengths, calculated in this work according to [19] and further described in section 2.3, and assuming that this length is invariant over time as described in the second assumption.

In order to evaluate the total corrosion damage from the initial current density and the corrosion-induced deflections measured by the DOFS, the deflection-time curve was discretized into smaller stages that can be approximated linearly. Therefore, based on the underlying hypothesis, the computation of current densities at later stages $i_j(k_j(t))$, when the slope of the deflection curve changes, could then be conducted according to Eq. (7):

$$i_j(k_j(t)) = i_1 \frac{k_j(t)}{k_1} \tag{7}$$

where k_1 is the slope of the incremental midspan deflection measured by the DOFS at the initiation of the corrosion process and $k_j(t)$ is the slope in later stages. This allows for the calculation of the total loss of steel volume in the pits C_{pits} through Faraday's law according to Eq. (8):

$$C_{pits} = \frac{MS_{pit}}{\rho F z} \int_0^t i_j(k_j(t))dt \tag{8}$$

where t is the time of applied current. It must be noted that if the initial current density is calculated using the surface area of the pits, as stated in Eq. (6), S_{pit} cancels out in Eq. (8) indicating that it is not necessary for determining the total volume loss. This means that the total volume of corrosion is independent of the area of steel assumed to be corroded but solely dependent on the applied current, which is typically unknown. However, it is relevant to highlight that the presented method requires an estimation of the effective pit length in order to transform corrosion-induced deflection values into corrosion rates that allow for the estimation of corrosion damages. Hence, if the initial corrosion rate is obtained by another method that does not rely on the actual knowledge of the corrosion distribution, e.g. 3D scanning results, an assumption of the pit length would be needed. Therefore, additional methods outside the scope of this work, are necessary to define the validity of such initial estimation. As an example of such methods, field measurements of the current densities at the affected cracks together with non-linear finite element analyses (NLFEA) iteratively combined could lead to a robust process to validate such estimation of the effective pit length until agreement between DOFS-calculated and NLFEA deflections is meet. However, the goal of the presented work is not to delve into such processes but to demonstrate that given an accurate estimation of such parameter, which in this work is done by the use of 3D scanning methods, the relation between corrosion-induced deflections and total corrosion damage is unequivocally defined by Eqs. (7) and (8), and only the corrosion at these regions is responsible to corrosion-induced

deflections.

Following the methodology outlined in [14], the deflection was obtained through double integration of the curvature $\chi(x)$, computed from the measured strains by DOFS according to Eq. (9):

$$\chi(x) = \frac{\varepsilon_{bot}(x) - \varepsilon_{top}(x)}{z} \tag{9}$$

where $\varepsilon_{bot}(x)$ and $\varepsilon_{top}(x)$ are the measured strains at the bottom and top reinforcement respectively and z is the vertical distance between the position of the DOFS.

4. Results and discussion

4.1. Validation of the framework for the case with imposed relative displacement

The correlation between localized pitting corrosion and increased deflection for the case with imposed relative displacement was studied in [21] and is summarized in this section as a validation of the framework presented in Section 3. Given that a constant relative displacement was enforced between the beams and considering that loading was applied approximately at an age of 1.5 years, creep deformations were expected to be small and similar for both beams as they were subjected to the same environmental conditions and same load levels. Therefore, it could be claimed that underlying hypothesis remained valid during the test and therefore, the measured variations in deflection were only due to the pitting corrosion, i.e. corrosion-induced deflections.

The total corrosion volume from the 3D scanning, $C_{tot,scan} = 12124$ mm^3, was used to calculate the effective impressed current $I_{eff} = 0.072$ A according to Eq. (5), and the initial current density i_1 was subsequently computed according to Eq. (6). The incremental deflection curve obtained from the DOFS measurements could then be used to calculate the later current densities according to Eq. (7). Subsequently, Eq. (8) was applied to calculate the volume loss due to corrosion in the pits at several times during the tests, namely whenever a clear change of stiffness was observed in the load-incremental deflection diagram. The results from these calculations are presented in Fig. 3, with the shaded region indicating the two-week period during which the impressed current ceased. In Fig. 3a, the incremental midspan deflection measured by the DOFS is presented, with the corresponding idealized deflection curve and slopes shown in Fig. 3b. The current densities at different stages are displayed in Fig. 3c and Fig. 3d shows the calculated volume losses in the pits throughout the accelerated corrosion test. The final calculated value of $C_{tot,pit} = 4989$ mm^3, resulted in a 2 % higher corrosion level than the measured value obtained from the 3D scanning, $C_{pit,scan} = 4893$ mm^3.

The deflections measured by the DOFS combined with the findings from [19], where the development of longitudinal cracks for the same beam was investigated, revealed that the slope of the deflection curve decreased when the first longitudinal crack appeared, namely at 14.8 days. This observation aligns with the assumption assuming the applied current, and thus all corrosion, concentrates at the pits during the initial phase of the corrosion process. The presence of longitudinal cracks enables the dispersion of the impressed current along the reinforcement bar, thereby reducing the current density and consequently the rate of pitting corrosion. With the applied current held constant, the overall deterioration rate remains constant as well. However, the increase of deflection is governed by the volume loss in the pits, as indicated by the reduction in slopes when the current density decreases. Furthermore, the incremental deflection ceased during the two weeks without impressed current, verifying the hypothesis stating that any observed variation in deflection can be ascribed to corrosion.

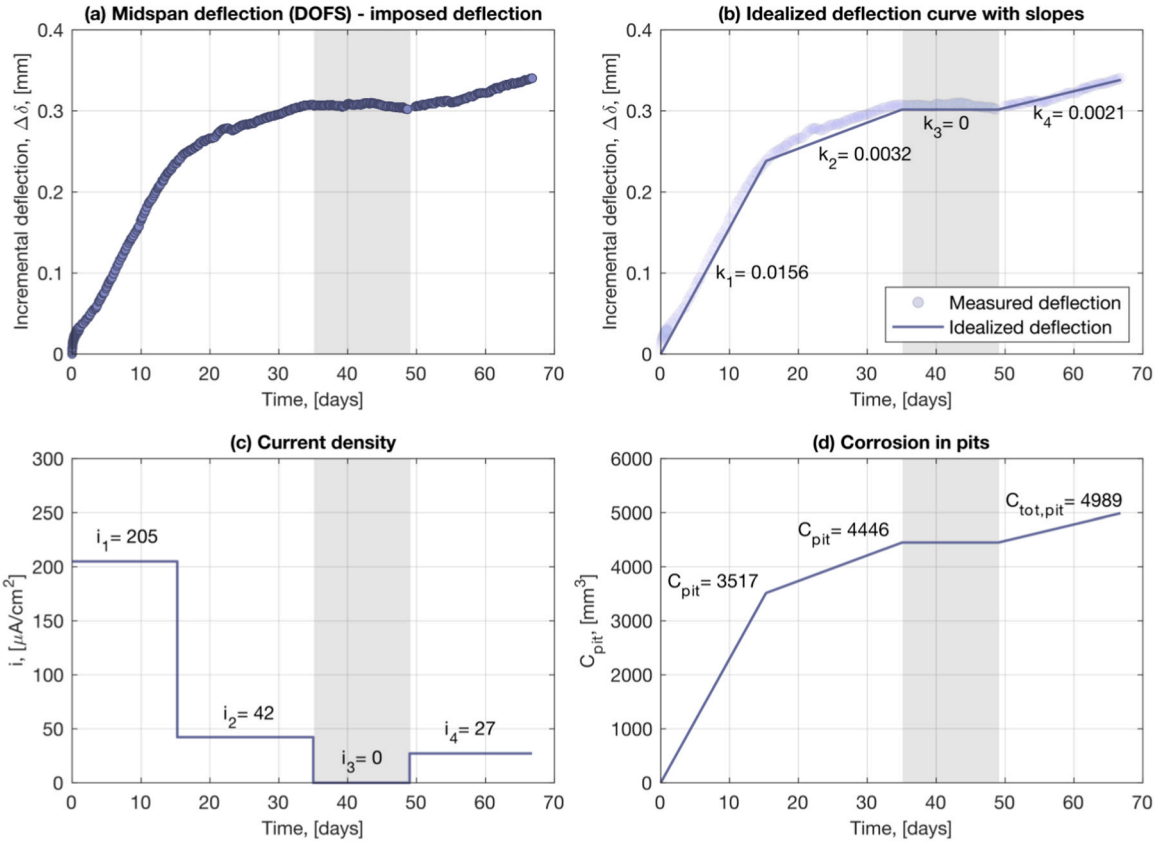

Fig. 3. **(a)** Midspan deflection measured by the DOFS for the beam subjected to an imposed relative displacement; **(b)** An idealized curve of the deflection with the slopes of each stage; **(c)** Current densities for the different stages. **(d)** Total corrosion in the pits calculated with Faraday's law.

4.2. Investigation of the framework's application for the case with cyclic loading

In this section the application of the framework for the case with cyclic loading is studied. In contrast to the imposed relative displacement case, the corrosion-induced deflection is not explicitly given by the DOFS measurements, and a more thorough investigation of the deflection variations is necessary.

4.2.1. Results from the 3D scanning

The corrosion volumes obtained from the 3D scanning and the subsequent surface interpolation of the point-cloud, as outlined in Section 2.3, were used to calculate an effective impressed current and subsequently the initial current density. The results are presented in Fig. 4, alongside the principal strain field derived from the DIC and the strains measured by the DOFS in bar 3 at the maximum load level.

Within the central region of the beam, seven distinct bending cracks were identified from the strain profile of the front bar, shown in Fig. 4b. The strains were verified with the results from the DIC in Fig. 4a, in which the cracks are numbered 1 to 7. Fig. 4c, Fig. 4d, and Fig. 4e illustrate the maximum corrosion level and pit volume for the front, middle and back bar respectively.

The experimental setup's success in inducing a non-uniform distribution with localized pitting corrosion through accelerated corrosion was validated by the results obtained from the 3D scanning. Furthermore, the pits corresponded well with the positions of the bending cracks, highlighting their influence on the localized corrosion.

The effective impressed current was calculated using Eq. (5), with a total corrosion volume of $C_{tot,scan} = 9709\ \text{mm}^3$, as $I_{eff} = 0.058$ A, in contrast to the actual applied current of 0.1 A. With the effective impressed current and the sum of pit lengths, $\sum L_{pit} = 552$ mm, the initial current density could be computed according to Eq. (6).

In Fig. 5, the pit lengths are depicted as a function of crack spacing and crack widths, based on the cracks shown in Fig. 4a. The crack spacing in Fig. 5a is defined as the distance from the midpoints to the adjacent cracks. In Fig. 5b, the crack widths obtained from the DIC at the end of the pre-cracking stage, before the corrosion experiment started, are shown as a function of the pit length. There is no clear correlation between either the crack width or the crack spacing and the pit length. However, the results in Fig. 5b indicate that the pit length was limited to the range of 16–32 mm, which corresponds to 1–2 bar diameters. Since the pit lengths in this study were obtained from the 3D scanner, which cannot be utilized in practical engineering situations, a better approach could be to use an average value, such as 1.5 bar diameters. However, further investigations are needed to verify the validity of this assumption and propose methods to estimate values of the pit length.

4.2.2. Corrosion-induced variations in deflection

The midspan deflections measured by the DOFS were studied to calculate the current densities in the later stages. The midspan deflection of the beam subjected to cyclic loading and accelerated corrosion, as illustrated in Fig. 6b, exhibits a similar increase in deflection during low-load level of the cycles, $F_L = 6$ kN, as observed in the case with imposed relative displacement. However, at the maximum load, $F_H = 36$ kN, the same pattern is not evident. Instead, the deflection is comparable to that of the uncorroded beam, as depicted in Fig. 6a, where the slight increase over time might be attributed to creep.

The correlation between the applied load level and the increment in midspan deflection, due to corrosion, becomes more apparent by the representation of the load-deflection curves shown in Fig. 7a and Fig. 7b for the uncorroded and corroded beam, respectively.

In the initial stage of the accelerated corrosion test, the deflections exhibit a linear correlation with the load level for both beams. However, with the progression of the corrosion penetration over time, the deflection increases, an increase that becomes more apparent as the load level decreases, as illustrated in Fig. 7b.

Therefore, to calculate the current densities according to Eq. (7), only the deflections for $F_L = 6$ kN were considered, corresponding to the fraction of the load that was permanently applied. Subsequently, the steel volume loss resulting from pitting corrosion was calculated according to Eq. (8). The results are presented in Fig. 8.

In Fig. 8a, midspan deflections during low load cycles, recorded by the DOFS, are presented with the first load cycle's deflection subtracted. Furthermore, deformations attributed to creep have been removed using results from the uncorroded beam, shown in Fig. 6a. The two-week period when the impressed current ceased is denoted by the shaded area. Fig. 8b illustrates an idealized deflection curve, accompanied by the slopes utilized for determining proportional current densities presented in Fig. 8c. Finally, Fig. 8d displays the total corrosion in all pits as a function of time, with a final value of $C_{tot,pit} = 3450\ \text{mm}^3$ at the conclusion of the accelerated corrosion test. This yielded a calculated corrosion level 0.5 % higher than the corresponding measured value obtained from the 3D scanning, $C_{pit,scan} = 3433\ \text{mm}^3$.

As for the case with imposed relative displacement, the findings firmly establish a correlation between increased deflection and localized pitting corrosion during the lower load cycles. While the simultaneous appearance of longitudinal cracks and reduction in the slope of the deflection curve has not been explicitly verified in the case of cyclic loading, the conclusions presented in Section 4.1 suggest that the same holds true in this scenario.

Further comparison of the cyclic loading and imposed relative displacement case reveals that the maximum incremental deflection was nearly five times larger in the case with cyclic loading, 1.65 mm, compared to 0.34 mm for the imposed relative displacement, as shown in Fig. 9a. However, in Fig. 9b, the total volume loss in the pits obtained from the 3D scanning accounted for only 70 % of the corresponding value for the imposed relative displacement, 3433 mm^3 and 4893 mm^3, respectively. These findings suggest the existence of another mechanism contributing to the increased deflection, in addition to the reduced stiffness due to the pitting corrosion. However, despite the difference in magnitude, the results suggest the second mechanism is still proportional to the corrosion rate. A possible explanation is that bond degradation is contributing to the increased deflection at lower load levels.

4.2.3. Mechanisms behind the corrosion-induced variations in deflection

As discussed in Section 4.2.2, a correlation between the corrosion development and the increase in deflection is argued for. In this section, the relation between the cyclic load level and increased deflection is further studied to explain why there is no increase in deflection for $F_H = 36$ kN. A deeper discussion of the measured strains is given, focusing on identifying differences in strain development between corroded and uncorroded specimens at different load levels, followed by a discussion of the influence of intermediate higher load cycles on the strain evolution, to support the hypothesis that bond degradation contributes to the increased deflection at lower load levels.

To identify contrasting responses in the strain evolution, measured at the location of the top and bottom reinforcement, the strain along the bar length and the strain evolution from day 0 to day 67 are illustrated in Fig. 10 and Fig. 11. Fig. 10 presents the front bar strains in the constant moment region, subjected to corrosion at the maximum load-level, $F_H = 36$ kN, for both the corroded and uncorroded beams, while Fig. 11 presents the strains at the minimum load-level, $F_L = 6$ kN.

For the uncorroded beam, at $F_H = 36$ kN, the results in Fig. 10a and Fig. 10c indicate a decrease in both bottom and top strains. The slightly more pronounced decrease in the bottom strains explains the gradual increase in deflection over time, as depicted in Fig. 6a and computed by Eq. (9). A dissimilar pattern is observed in the strains of the corroded beam, as presented in Fig. 10b. In this case, the strains are distributed such that the bottom strains, shown in Fig. 10d, increase, while top strains tend towards more positive values. However, at the first crack, the bottom strains decrease instead. This deviation could potentially be attributed to the minimal occurrence of pit corrosion, as depicted by

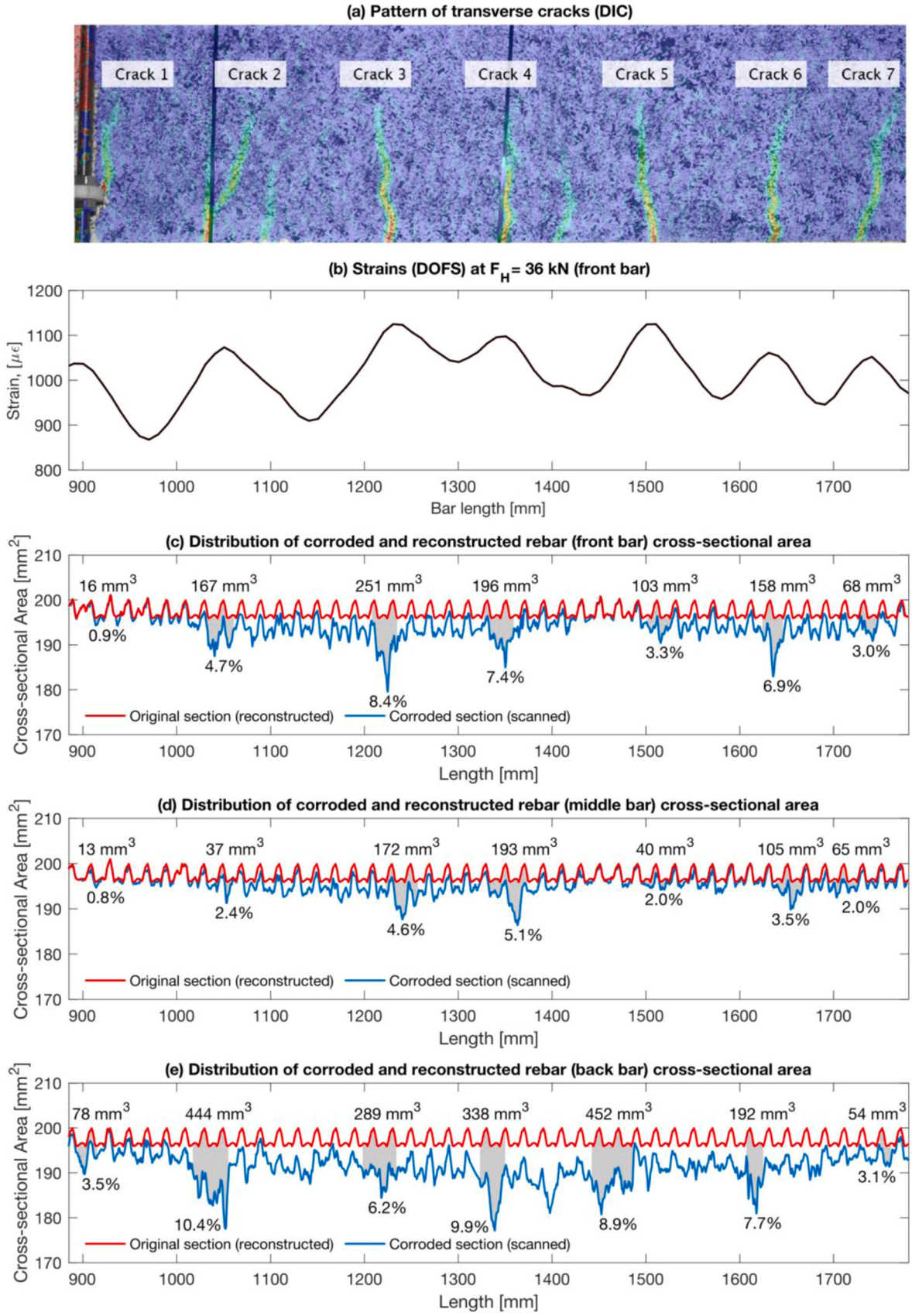

Fig. 4. **(a)** Position of bending cracks measured by DIC; **(b)** Strains in bar 3 for a load cycle with maximum load, $F_H = 36$ kN; **(c, d, e)** Variation of residual and original cross-sectional area along the rebars, together with pit volume and maximum corrosion level of each pit.

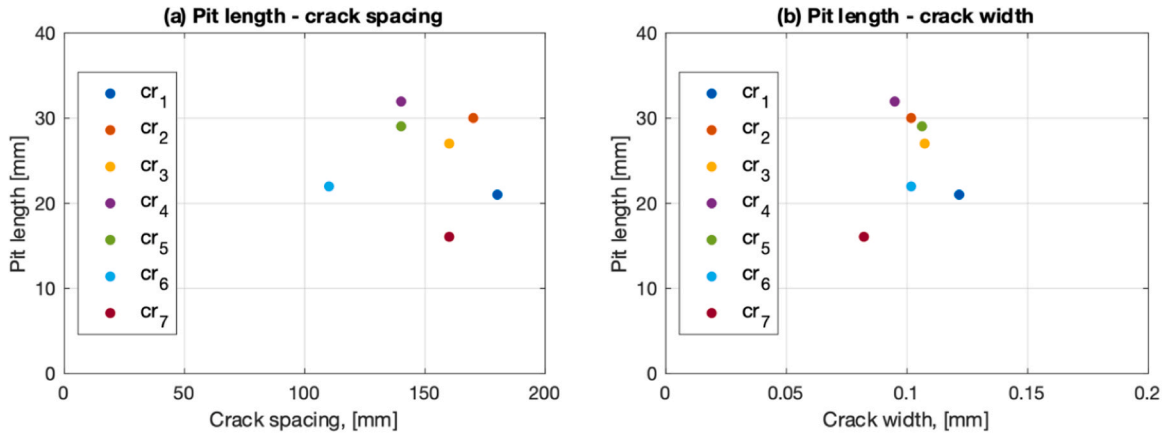

Fig. 5. **(a)** Pit length as a function of the crack spacing; **(b)** Pit length as a function of the crack width.

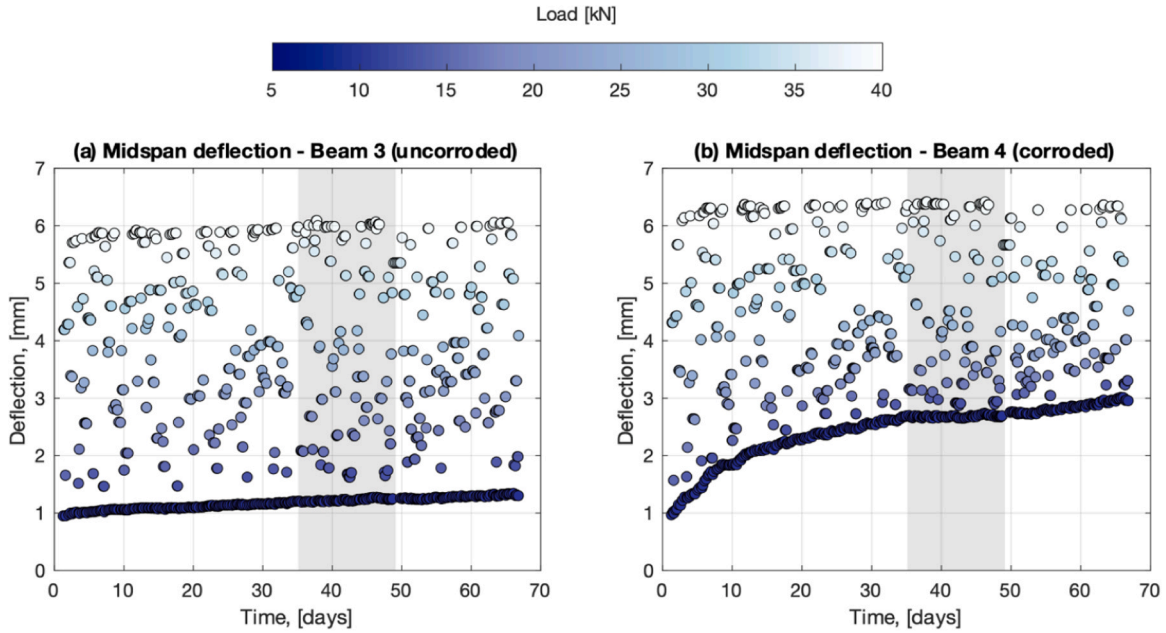

Fig. 6. **(a)** Midspan deflection measured by the DOFS for the uncorroded reference beam subjected to cyclic loading; **(b)** Midspan deflection measured by the DOFS for the beam subjected to accelerated corrosion and cyclic loading.

Fig. 4c, and may indicate a distribution of curvature towards the constant moment region.

The front bar strains within the constant moment region measured by the top and bottom DOFS at $F_L = 6$ kN are presented in Fig. 11, for the corroded and uncorroded beams, respectively.

As for the strains in the uncorroded beam, the results are similar to the strains at $F_H = 36$ kN, with the top strains exhibiting a more substantial decrease than the bottom strains. In Fig. 11a and Fig. 11c, the zoomed-in regions illustrate the evolution of midspan strains during the extended period of loading, with similar scales on the y-axis. It becomes evident that the increased deflections are attributed to creep, as it is the concrete in compression that undergoes creep strains.

The evolution of top strains in the corroded beam, shown in Fig. 11b, resembles those observed at the maximum load level, while the bottom strains, presented in Fig. 11d, significantly increase compared to Fig. 10d, explaining the increased deflection at $F_L = 6$ kN. Furthermore, the observed flattening of peaks and valleys in the bottom strains suggests a lack of contribution from the concrete between the cracks due to bond. This is not the case at higher load levels, indicating that bond degradation occurs only when the load surpasses a previous threshold in combination with corrosion.

To further investigate the relation between corrosion, possible bond degradation and strain evolution, two cyclic loading sequences at $F_H = 18$ kN and $F_H = 19$ kN, are studied in detail: one case in which three sequential load levels are at approximately the same load ($F_H = 18$ kN) in Fig. 12, and one case in which the sequence of $F_H = 19$ kN loads is interrupted by a significantly higher F_H, in Fig. 13.

First, the strains associated with three load cycles, $F_H = 18$ kN shown in Fig. 12a, are studied. The strains in the uncorroded beam, illustrated in Fig. 12b, experience a slight increase due to a marginal difference in the load level during the last load cycle. However, in the corroded beam, the strains shown in Fig. 12c do not increase, which would have been the case in the presence of bond degradation.

Fig. 13 depicts a situation similar to Fig. 12, but with the difference that it involves two intermediate load cycles with a higher load level. Load cycles over the period of 59 days and 61 days are illustrated in Fig. 13a, while the corresponding strains for the load level $F_H = 19$ kN are displayed in Fig. 13b and Fig. 13c for the uncorroded and corroded beams, respectively. For the case with higher loads in between, the strains in the uncorroded beam experience once more a slight variation

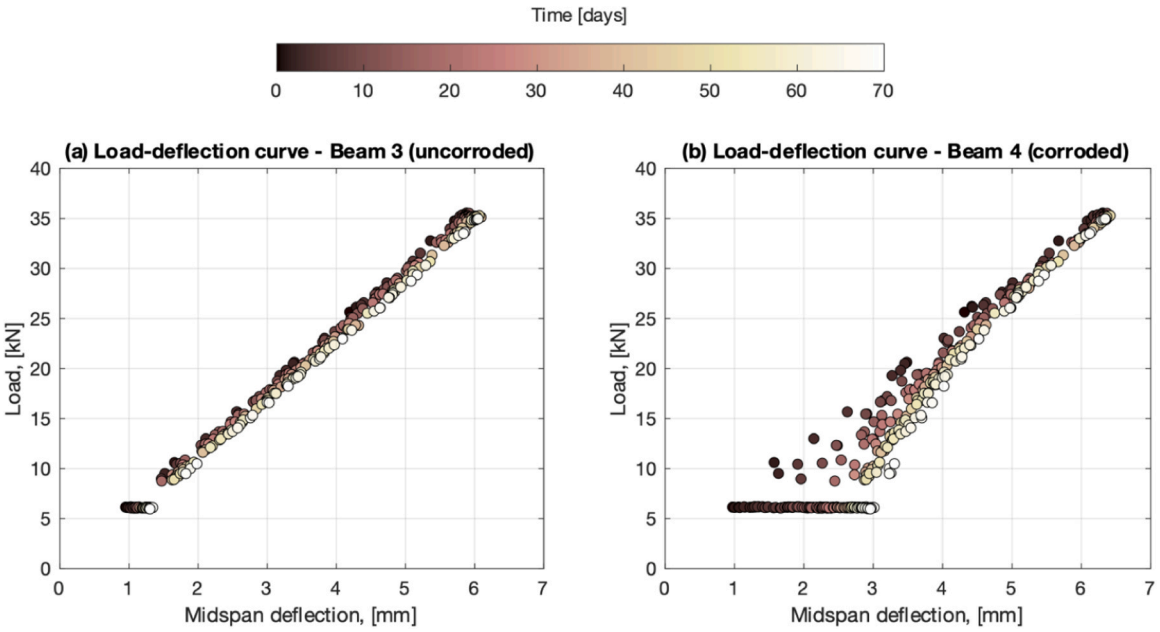

Fig. 7. **(a)** Load-deflection curve for the uncorroded reference beam subjected to cyclic loading; **(b)** Load-deflection curve for the beam subjected to accelerated corrosion and cyclic loading.

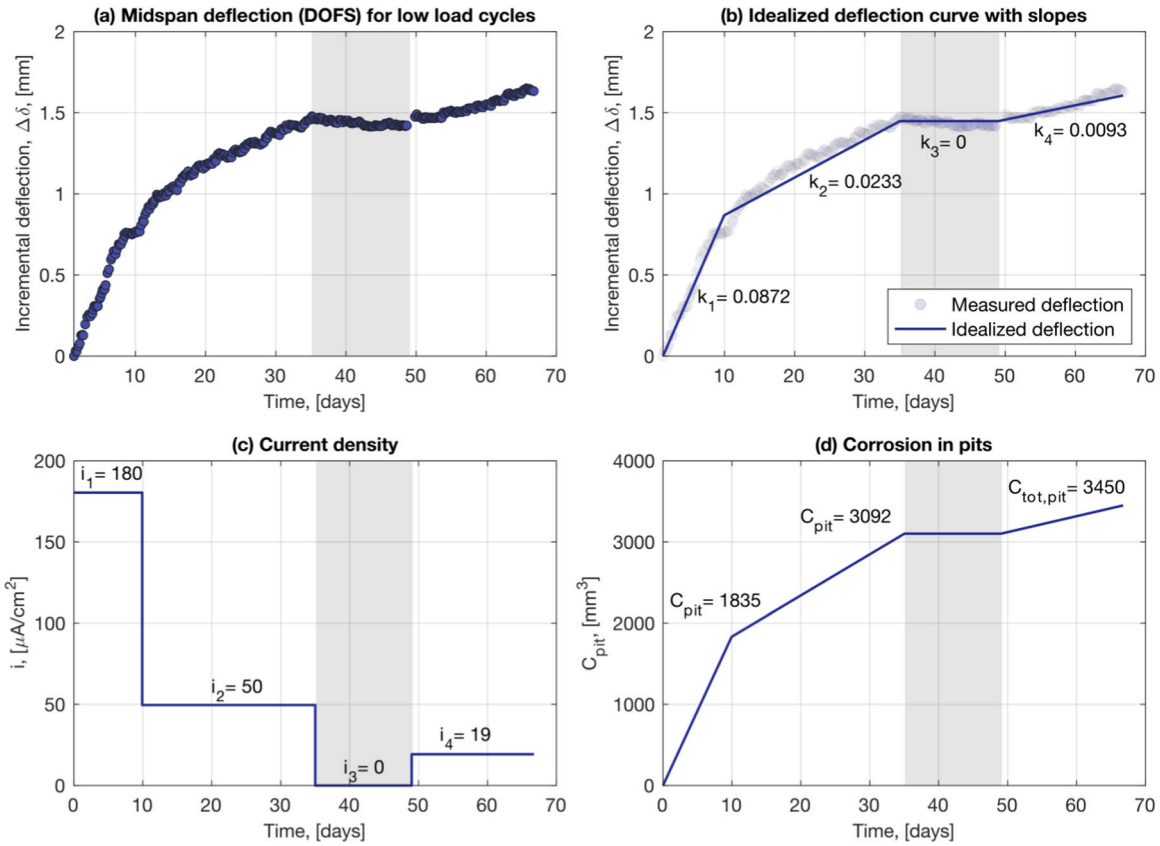

Fig. 8. **(a)** Midspan deflection measured by the DOFS for low load cycles, $F_L = 6$ kN; **(b)** An idealized curve of the deflection with the slopes of each stage; **(c)** Current densities for the different stages; **(d)** Total corrosion in the pits calculated with Faraday's law.

due to marginal differences in the load level during the load cycles. However, in contrast to the first case a considerable increase in strains is observed in the corroded beam, compared to the uncorroded beam subsequent to the higher load cycles. This observation aligns with the hypothesis that bond degradation occurs only when the load surpasses a previous level in combination with corrosion.

5. Conclusions

In this paper, a framework for describing corrosion propagation from

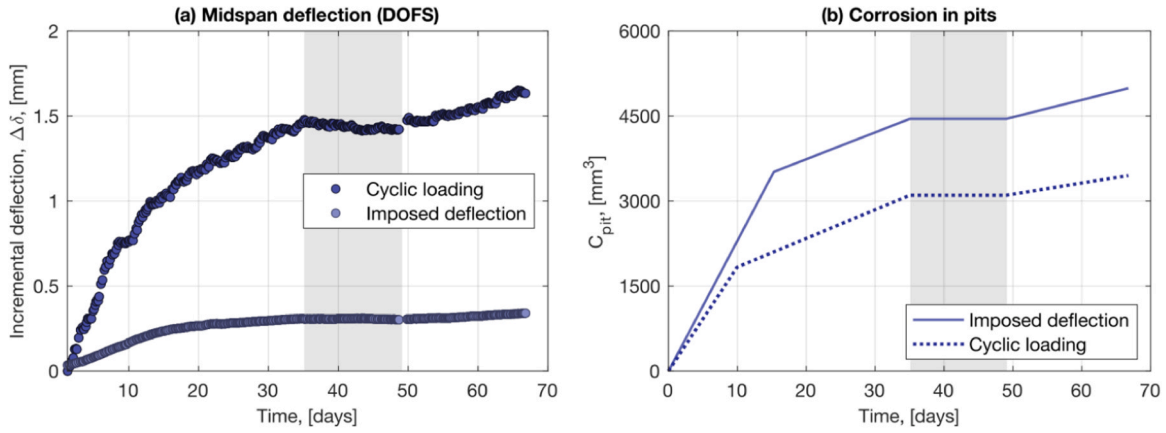

Fig. 9. **(a)** Comparison of midspan deflection measured by the DOFS for imposed relative displacement and low load cycles, $F_L = 6$ kN; **(b)** Comparison of total corrosion in the pits, calculated with Faraday's law, for imposed relative displacement and low load cycles, $F_L = 6$ kN.

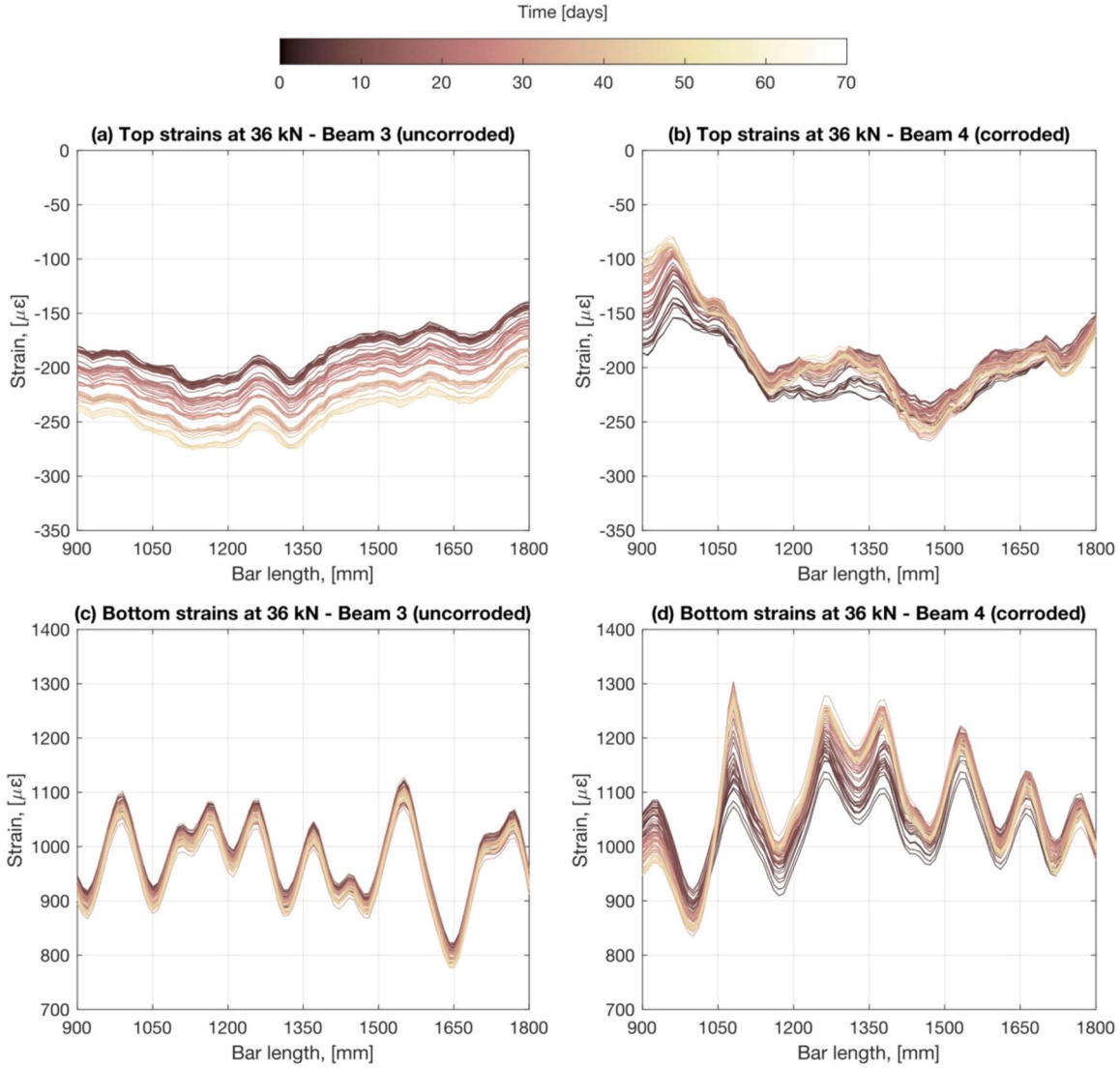

Fig. 10. **(a, b)** Strains along the top reinforcement bar for load cycles $F_H = 36$ kN, in the uncorroded and corroded beam, respectively; **(c, d)** Strains along the bottom reinforcement bar for load cycles $F_H = 36$ kN, in the uncorroded and corroded beam, respectively.

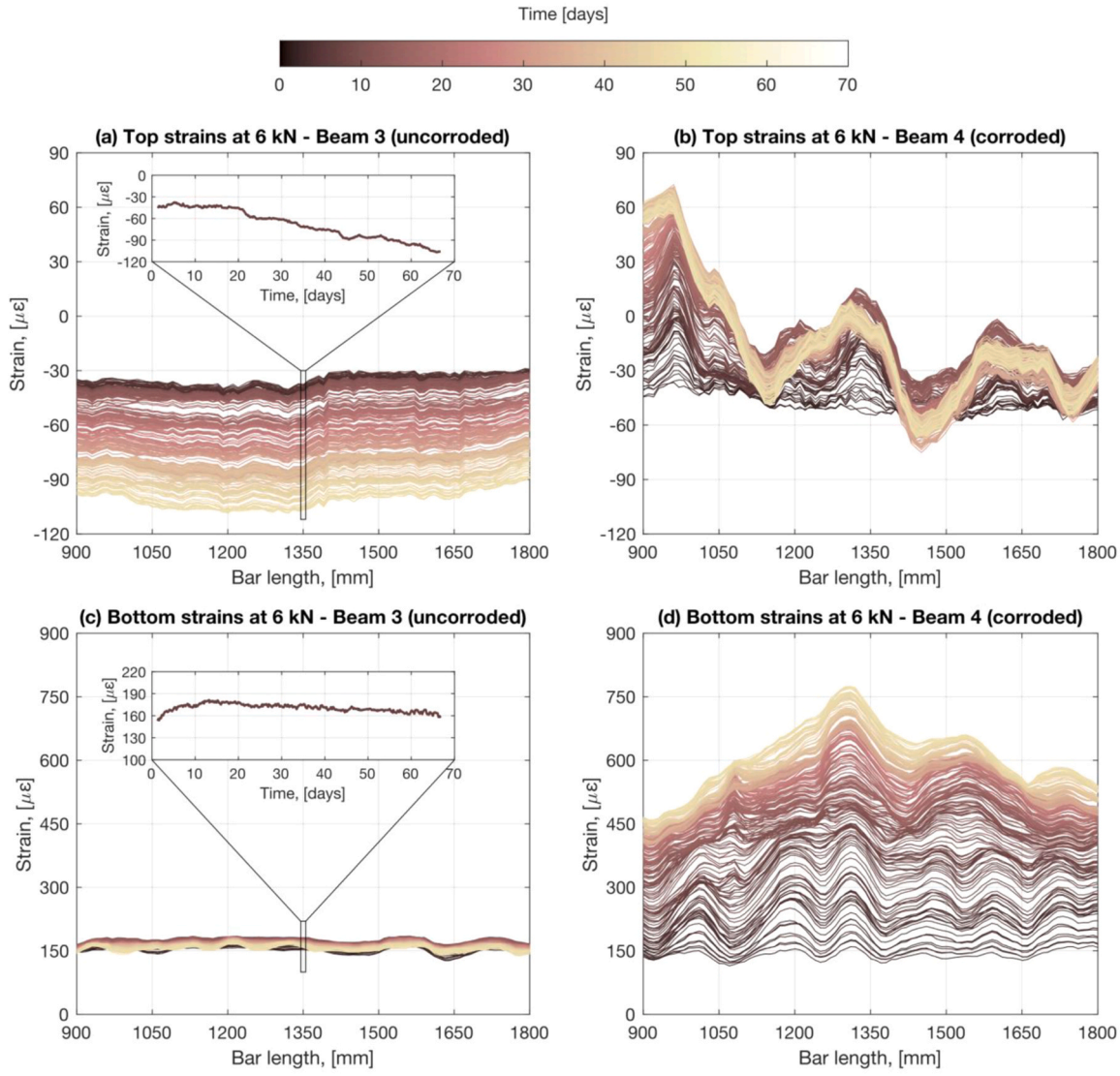

Fig. 11. (a, b) Strains along the top reinforcement bar for load cycles $F_L = 6$ kN, in the uncorroded and corroded beam, respectively; **(c, d)** Strains along the bottom reinforcement bar for load cycles $F_L = 6$ kN in the uncorroded and corroded beam, respectively.

corrosion-induced variations in deflection for RC beams was proposed. The framework was verified for a beam subjected to an imposed relative displacement with respect to an uncorroded reference beam, where the measured variations in deflection could be attributed solely to the loss of local cross-section in the steel reinforcement. Subsequently, the application of the framework to the case of a RC beam simultaneously subjected to pitting corrosion and cyclic loading was investigated. The main conclusions drawn from this study are the following:

- The proposed framework establishes a direct correlation between the observed variation rate of corrosion-induced deflections and the local mass loss rate at the corrosion pits in beams with localized pitting corrosion.

- The framework was verified at the end of the corrosion process as revealed by the strong agreement between the pit volume loss obtained from the 3D scanning and the losses calculated using Faraday's law. This held true for the case with imposed relative displacement and also for the case with cyclic loading when the incremental deflection for the lowest load cycles was considered in the calculations.

- Unlike other methods to estimate corrosion damages, the current framework allows for a time-based description of the damages, based solely on the deflection measurements. However, as is typical for such methods, the accuracy of the framework is highly dependent on the knowledge of the corrosion rate. Moreover, the pit lengths are needed when converting global damage to local damage. When this information is known, e.g. from 3D scanning results, the agreement was demonstrated to be excellent. Nevertheless, in common cases where pit lengths cannot be acquired through 3D scanning of the reinforcement bars, alternative methods are needed to establish such values.
- Furthermore, it is relevant to indicate that the presented method only requires the estimation of one corrosion rate, preferably prior to the formation of corrosion-induced longitudinal cracks, in order to evaluate the corrosion damages during the entire structure's service life.
- The results from the 3D scanning did not indicate a strong correlation between crack width and pit length, with pit lengths limited to the range of 1-2 bar diameters. Further research is needed to establish better correlations.
- A second mechanism contributing to corrosion-induced variations in deflection, in addition to the reduced stiffness due to pitting

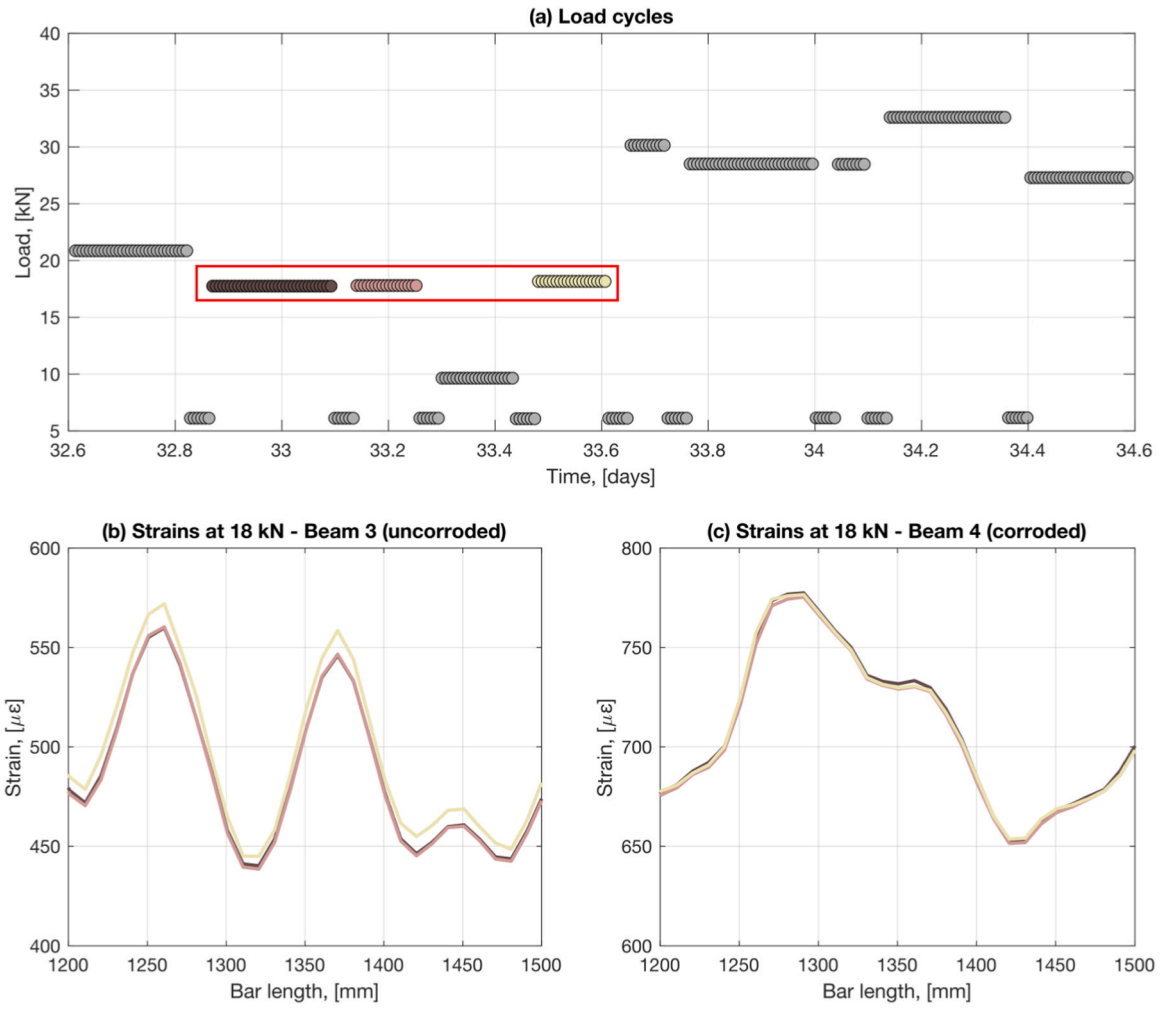

Fig. 12. **(a)** Load cycles in the time span between 32.6 days and 34.6 days; **(b, c)** Strains along the bottom reinforcement bar for load cycles $F_H = 18$ kN, for the uncorroded and corroded beam respectively.

corrosion, was observed for the case with cyclic loading since the incremental deflection was five times higher with only 70 % of steel loss, compared to the beam subjected to an imposed relative displacement. This was attributed to bond degradation due to the flattening of peaks and valleys in the strain profiles of the reinforcement as the corrosion rate increased.

- In the beam subjected to cyclic loading and corrosion, a correlation existed between the applied load levels and the corrosion-induced variations in deflection. For load cycles with a similar load level, it was shown that the increase in deflection occurred only when there were intermediate load cycles with a higher load level, indicating that the assumed bond degradation occurs only when the load surpasses a previous threshold.

In this study, 3D scanning of the reinforcement bars was used for validation of the framework. Further research is needed to enable the application of the framework without relying on the results from the 3D scanning of reinforcement bars. In this study, these results were used to determine the initial corrosion rate from the total volume loss together with the pit lengths. However, if the initial corrosion rate could be determined with another method, such as non-destructive testing or numerical modeling, the framework could be applicable to practical engineering situations as well. Moreover, the framework has only been verified for beams subjected to accelerated corrosion for a fixed time period of 67 days. Therefore, further research is needed to study how the pit lengths develop to verify the assumption that the pit lengths do not change significantly over time as well as for higher corrosion levels.

Funding

This research has been performed as part of the project: 'Shedding light on internal damage: fiber optic-driven condition assessment of corroded concrete structures' funded by the Swedish Government Research Council Formas under the grant 2021-01103_Formas.

CRediT authorship contribution statement

Carlos Gil Berrocal: Writing – review & editing, Writing – original draft, Visualization, Validation, Methodology, Investigation, Funding acquisition, Data curation, Conceptualization. **David Dackman:** Writing – original draft, Visualization, Methodology, Investigation, Formal analysis, Data curation. **Ignasi Fernandez:** Writing – review & editing, Writing – original draft, Supervision, Methodology, Funding acquisition, Formal analysis, Data curation, Conceptualization. **Rasmus Rempling:** Writing – review & editing, Writing – original draft, Methodology, Funding acquisition.

Declaration of Competing Interest

The authors declare that they have no known competing financial interests or personal relationships that could have appeared to influence the work reported in this paper.

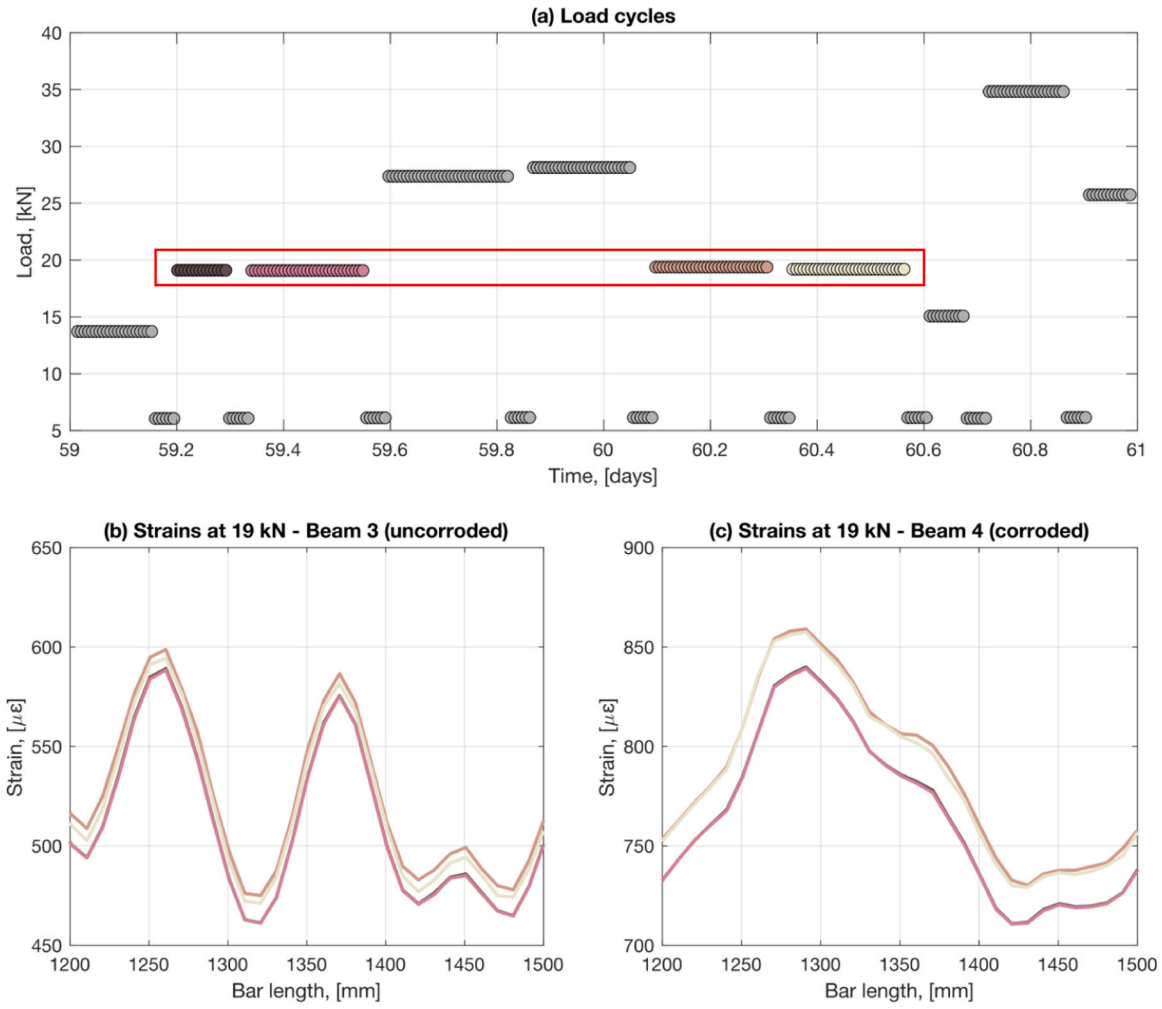

Fig. 13. **(a)** Load cycles in the time span between 59 days and 61 days; **(b, c)** Strains along the bottom reinforcement bar for load cycles $F_H = 19$ kN, for the uncorroded and corroded beam respectively.

Data Availability

Data will be made available on request.

References

[1] Bonacci JF, Maalej M. Externally-bonded FRP for service-life extension of RC infrastructure. J Infrastruct Syst 2000;vol. 6(1):41–51.

[2] Tahershamsi M, Fernandez I, Lundgren K, Zandi K. Investigating correlations between crack width, corrosion level and anchorage capacity. Struct Infrastruct Eng 2017;vol. 13(10):1294–307. https://doi.org/10.1080/15732479.2016.1263673.

[3] Hariche L, Ballim Y, Bouhicha M, Kenai S. Effects of reinforcement configuration and sustained load on the behaviour of reinforced concrete beams affected by reinforcing steel corrosion. Cem Concr Compos 2012;vol. 34(10):1202–9. https://doi.org/10.1016/j.cemconcomp.2012.07.010.

[4] Zhang R, Castel A, François R. The corrosion pattern of reinforcement and its influence on serviceability of reinforced concrete members in chloride environment. Cem Concr Res 2009;vol. 39(11):1077–86. https://doi.org/10.1016/j.cemconres.2009.07.025.

[5] Castro P, Véleva L, Balancán M. Corrosion of reinforced concrete in a tropical marine environment and in accelerated tests. Constr Build Mater 1997;vol. 11(2):75–81. https://doi.org/10.1016/S0950-0618(97)00009-3.

[6] Fang C, Lundgren K, Chen L, Zhu C. Corrosion influence on bond in reinforced concrete. Cem Concr Res Nov. 2004;vol. 34(11):2159–67. https://doi.org/10.1016/j.cemconres.2004.04.006.

[7] Law DW, Molyneaux TCK. Impact of corrosion on bond in uncracked concrete with confined and unconfined rebar. Constr Build Mater 2017;vol. 155:550–9. https://doi.org/10.1016/j.conbuildmat.2017.08.112.

[8] Du Y, Cullen M, Li C. Structural performance of RC beams under simultaneous loading and reinforcement corrosion. Constr Build Mater 2013;vol. 38:472–81. https://doi.org/10.1016/j.conbuildmat.2012.08.010.

[9] Stein KJ, Graeff ÂG, Garcez MR. Structural performance of reinforced concrete beams subjected to combined effects of corrosion and cyclic loading. J Build Pathol Rehabil Jun. 2023;vol. 8(1). https://doi.org/10.1007/s41024-022-00263-1.

[10] Fang C, Gylltoft K, Lundgren K, Plos M. Effect of corrosion on bond in reinforced concrete under cyclic loading. Cem Concr Res Mar. 2006;vol. 36(3):548–55. https://doi.org/10.1016/j.cemconres.2005.11.019.

[11] Oh BH, Asce M, Kim SH. Realistic models for local bond stress-slip of reinforced concrete under repeated loading. J Struct Eng 2007;vol. 133(2):216–24. https://doi.org/10.1061/ASCE0733-94452007133:2216.

[12] Zhou HJ, Liang XB, Zhang XL, Lu JL, Xing F, Mei L. Variation and degradation of steel and concrete bond performance with corroded stirrups. Constr Build Mater May 2017;vol. 138:56–68. https://doi.org/10.1016/j.conbuildmat.2017.02.007.

[13] Berrocal CG, Fernandez I, Rempling R. Crack monitoring in reinforced concrete beams by distributed optical fiber sensors. Struct Infrastruct Eng 2021;vol. 17(1):124–39. https://doi.org/10.1080/15732479.2020.1731558.

[14] Fernandez I, Berrocal CG, Rempling R. Long-term performance of distributed optical fiber sensors embedded in reinforced concrete beams under sustained deflection and cyclic loading. Sensors 2021;vol. 21(19). https://doi.org/10.3390/s21196338.

[15] Fernandez I, Berrocal CG, Rempling R. Two-dimensional strain field analysis of reinforced concrete D-regions based on distributed optical fibre sensors. Eng Struct Mar. 2023;vol. 278. https://doi.org/10.1016/j.engstruct.2022.115562.

[16] Bado MF, Casas JR, Kaklauskas G. Distributed Sensing (DOFS) in Reinforced Concrete members for reinforcement strain monitoring, crack detection and bond-slip calculation. Eng Struct Jan. 2021;vol. 226. https://doi.org/10.1016/j.engstruct.2020.111385.

[17] Fan L, Tan X, Zhang Q, Meng W, Chen G, Bao Y. Monitoring corrosion of steel bars in reinforced concrete based on helix strains measured from a distributed fiber optic sensor. Eng Struct Feb. 2020;vol. 204. https://doi.org/10.1016/j.engstruct.2019.110039.

[18] EN 12390–3:2009 Testing hardened concrete - Part 3: Compressive strength of test specimens, 2009.

[19] Berrocal CG, Fernandez I, Rempling R. The interplay between corrosion and cracks in reinforced concrete beams with non-uniform reinforcement corrosion. Mater

Struct/Mater Et Constr 2022;vol. 55(4):1–16. https://doi.org/10.1617/s11527-022-01956-2.

[20] Fernandez I, Lundgren K, Zandi K. Evaluation of corrosion level of naturally corroded bars using different cleaning methods, computed tomography, and 3D optical scanning. Mater Struct/Mater Et Constr 2018;vol. 51(3):1–13. https://doi.org/10.1617/s11527-018-1206-z.

[21] D. Dackman, I. Fernandez, C.G. Berrocal, and R. Rempling, Correlations between localized pitting corrosion and deflection in reinforced concrete beams subjected to accelerated corrosion, in International RILEM Conference on Synergising Expertise towards Sustainability and Robustness of Cement-based Materials and Concrete Structures, 2023, pp. 902–912.